Title
Assessment of microwave power flow for reflectometry measurements in tokamak plasmas

Journal
Plasma Physics and Controlled Fusion, 50(2)

ISSN
0741-3335

Authors
Gourdain, P-A
Peebles, W. A.

Publication Date
2008-02-01

DOI
10.1088/0741-3335/50/2/025004

Peer reviewed

Assessment of microwave power flow for reflectometry measurements in tokamak plasmas

P.-A. Gourdain[a], W. A. Peebles
Department of Physics and Astronomy
University of California Los Angeles, CA 90095-1547

Microwave diagnostics, such as reflectometry and electron cyclotron emission, are widely employed in tokamak fusion plasmas, and are also particularly well-suited to the burning plasma environment expected in the upcoming ITER device. In existing fusion plasmas, reflectometry has been used to measure electron density profile, density fluctuations, turbulent flow and internal magnetic field strength. The measurement of electron density profile via reflectometry is a particularly high priority in ITER, and so an assessment of electromagnetic wave propagation is important in estimating measurement capability. In ITER, the ratio of plasma size to the required microwave signal wavelength is significantly larger than in current fusion experiments ensuring a more realistic analysis of reflectometry via ray tracing techniques. The analytical and numerical studies presented in this paper highlight the fact that the group velocity (or power flow) is strongly dependent on the direction of wave propagation relative to the magnetic field. It is shown that this dependence strongly modifies power flow near the cut-off layer in a manner that embeds the local magnetic field direction in the "foot-print" of the returned power at the launch antenna. It will be shown that this can potentially be utilized to determine the magnetic field pitch angle at the cutoff location. The resultant beam drift and distortion due to the magnetic field also have consequences on the design of reflectometry systems for large, high-field fusion experiments such as ITER.

PACS: 52.55.Fa, 41.20.-q

[a] gourdain@ucla.edu

Introduction

Microwave measurements have been used to determine many important properties of fusion plasmas, such as density[1], magnetic field strength[2], fluctuations[3], and flows[4]. Diagnostic techniques, such as interferometry, electron cyclotron emission, collective scattering, and reflectometry have been widely employed. Reflectometry provides local measurement of a number of parameters and is one of the most important techniques – well-suited to application on ITER. In this technique microwave radiation propagates into the plasma at such a frequency that it meets a plasma cutoff and reflects back towards the launch antenna. If the spatial gradients of plasma density and magnetic field are small compared to the wavelength of the beam, one can model the propagation as rays of "microwave-light". The local properties of the refractive index N modify the ray trajectory. If the wave exchanges energy with the plasma due to resonance, damping occurs. In this case, the refractive index increases as the resonance is approached. On the other hand, when the waves become evanescent, the refractive index N approaches zero, and the waves reflect at what is called the "cutoff". Since there is reflection, the beam returns towards the microwave antenna. The amplitude and phase of this reflected radiation can then be processed to extract information on plasma density.

When modeling magnetized plasma, the medium is birefringent and the refractive index becomes dependent on magnetic field. In toroidal fusion research devices, such as tokamaks, microwave reflectometry typically utilizes a radial launch, where the wave propagates predominantly in the poloidal plane. If the electric field of the launched electromagnetic wave is polarized parallel to the magnetic field, this is known as "O-mode" reflectometry. If the electric field is perpendicular, it is referred to as "X-mode"

reflectometry. However, in reality, launch of pure O- or X-mode radiation is not possible in a magnetized plasma due to beam divergence. In addition, in a tokamak plasma the magnetic field helicity also prevents pure O- or X-mode propagation. As is well-known, tokamaks have a magnetic field with components in the toroidal (i.e. axisymmetric) direction and poloidal (i.e. vertical) plane. The field direction is not homogeneous since the poloidal field varies significantly across the whole plasma volume. In addition, as mentioned above, a microwave beam with finite cross-section has intrinsic divergence which ensures that there will be a variation in the angle made with the magnetic field. As a result, a beam in a tokamak cannot traverse an extended spatial region at a constant angle to the internal magnetic field. The resultant non-uniformities in refractive index stir and distort the beam as it progresses through the plasma.

In this paper, we evaluate analytically, as well as numerically, the effects of this intrinsic misalignment between wave propagation and confining magnetic field. The physical model that determines wave propagation is described, with particular emphasis on the dispersion relation and associated cut-off frequencies. The energy flow is initially modeled as a single ray. The distortion of the whole cross-section of the beam is then determined analytically by representing the beam as a pencil of rays. The importance of accounting for beam drift and distortion in the design of reflectometer systems for large and high-field tokamaks such as ITER is discussed. Finally, the analytically predicted beam drift and distortion are confirmed numerically. It is shown that these modifications have the potential to determine magnetic field pitch angle at cut-off.

Physical Model

In the cold plasma approximation, the dispersion relation, D, is given[5] by

$$D = AN^4 - BN^2 + C \tag{1}$$

with

$$\begin{cases} A = \left[K_\perp \sin^2\theta + K_\parallel \cos^2\theta \right] \\ B = \left[\left(K_\perp^2 - K_\times^2 \right) \sin^2\theta + K_\parallel K_\perp \left(1 + \cos^2\theta \right) \right], \\ C = K_\parallel \left(K_\perp^2 - K_\times^2 \right) \end{cases} \tag{2}$$

and

$$\mathbf{N} = \frac{c}{\omega}\mathbf{k} \,. \tag{3}$$

N is the refractive index vector, c the speed of light in vacuum, ω the angular frequency of the propagating wave, **k** the angular wave number (propagation) vector, θ the angle between **k** and the non-oscillating (i.e. main) magnetic field **B.**

"cos θ" is usually expressed independently of any coordinate system by using Eq. (4),

$$\cos^2\theta = \frac{1}{\mathbf{N}.\mathbf{N}} \frac{1}{\mathbf{B}.\mathbf{B}} \left(\mathbf{N}.\mathbf{B} \right)^2 . \tag{4}$$

If we restrict ourselves to a single species (electron) plasma we have

$$K_\perp = 1 - \frac{\Pi_e^2}{\omega^2 - \Omega_e^2}, \; K_\times = -\frac{\Pi_e^2}{\omega^2 - \Omega_e^2} \frac{\Omega_e}{\omega} \text{ and } K_\parallel = 1 - \frac{\Pi_e^2}{\omega^2}, \tag{5}$$

using Π_e for the electron plasma frequency and Ω_e for the electron cyclotron frequency.

$D = 0$ is a necessity for wave propagation[5], so any propagating (as opposed to evanescent) wave in a plasma satisfies

$$\left(AN^2 - B \right) N^2 = -C \tag{6}$$

Wave cut-off is obtained when is $N = 0$. Hence Eq. (6) shows that a necessary condition to wave cut-off is $C = 0$, yielding

$$K_\perp^2 = K_\times^2 \text{ or } K_\parallel = 0 \,. \tag{7}$$

The first equality of Eq. (7) gives the upper (*U*) and lower (*L*) cut-off frequencies

$$\omega_U = \frac{\Omega_e}{2} + \sqrt{\frac{\Omega_e^2}{4} + \Pi_e^2} \text{ and } \omega_L = -\frac{\Omega_e}{2} + \sqrt{\frac{\Omega_e^2}{4} + \Pi_e^2}\,, \tag{8}$$

used in X-mode reflectometry, while the second equality gives the plasma cut-off frequency used in O-mode reflectometry.

$$\omega_O = \Pi_e\,, \tag{9}$$

In fusion devices such as ITER, the wavelength of the microwave radiation is generally much smaller than the distance over which the refractive index changes appreciably. Hence it is possible to use the geometrical ray tracing approximation[6] when solving the wave equation. Then the space-time trajectory of the beam is given by

$$\frac{d\mathbf{r}}{ds} = \frac{\partial D}{\partial \mathbf{k}} \text{ and } \frac{dt}{ds} = -\frac{\partial D}{\partial \omega}\,. \tag{10}$$

where *s* is the distance along the ray and **r** is the position vector along this ray. While **k** and ω vary according to the change in **r**, they always satisfy the propagation equation D = 0 giving

$$\frac{d\mathbf{k}}{ds} = -\frac{\partial D}{\partial \mathbf{r}} \text{ and } \frac{d\omega}{ds} = -\frac{\partial D}{\partial t}\,. \tag{11}$$

The ray trajectory corresponds to the flow of power (or group velocity) of the beam and follows the equation

$$\frac{d\mathbf{r}}{dt} = \mathbf{v}_g\,. \tag{12}$$

The group velocity can then be recast as

$$\mathbf{v}_g = -\frac{\partial D / \partial \mathbf{k}}{\partial D / \partial \omega} = -\frac{\partial \omega}{\partial \mathbf{k}}\,. \tag{13}$$

The reader should remember that the *wave* propagates parallel to the phase velocity $\mathbf{v}_{ph}$, while the beam trajectory (or flow of power) is parallel to the group velocity $\mathbf{v}_g$. Since we

use ray tracing, the remainder of this paper will focus on understanding the power flow in terms of the group velocity. As the cut-off is approached the incident microwave wavelength increases theoretically approaching infinity at the cutoff. Nevertheless near the cut-off layer, full wave codes show that the effective wavelength of the microwaves typically increases by less than an order of magnitude before reflection. As a consequence, in this paper it is assumed that the ray tracing approximation is still valid "near" the cut-off layer. When considering a ray tracing model, the natural inclination is first to represent the whole beam as a single ray as described in the following section.

Single ray model

In this section, the global cylindrical coordinate system (R, Z, ϕ) is utilized. The toroidal axisymmetric direction is defined by the ϕ-direction, while the vertical (poloidal) plane is defined by the (R, Z) plane. We write $\mathbf{B} = (B_R, B_Z, B_\phi)$, $v_g = (dR/dt.\ dZ/dt.\ Rd\phi/dt)$ and $\mathbf{N} = (N_R, N_Z, N_\phi)$. We use $\mathbf{N}$ instead of $\mathbf{k}$ for the propagation direction since $\mathbf{N}$ appears naturally in all the following equations. The group velocity $v_{g,\chi}$ in the χ-direction (χ being R, Z or ϕ) has the following form

$$v_{g,\chi} = \frac{c\omega^2\left(\omega^2-\Omega_e^2\right)\left[\begin{array}{l}\mathbf{B}.\mathbf{N}\left(B_\chi\left[1-\mathbf{N}^2\right]-N_\chi\mathbf{B}.\mathbf{N}\right)\Omega_e^2\Pi_e^2+\\ \mathbf{B}^2N_\chi\left(\begin{array}{l}2\left[\Pi_e^2-\omega^2\right]\left[\Pi_e^2+\left(\mathbf{N}^2-1\right)\omega^2\right]+\\ \left[\Pi_e^2+2\left(\mathbf{N}^2-1\right)\omega^2\right]\Omega_e^2\end{array}\right)\end{array}\right]}{\Pi_e^2\left[\begin{array}{l}\left(1-\mathbf{N}^2\right)\left(\mathbf{B}.\mathbf{N}\right)^2\omega^2\Omega_e^2\left(2\omega^2-\Omega_e^2\right)+\\ \mathbf{B}^2\left(\begin{array}{l}\Pi_e^4\left[3\omega^2-2\Omega_e^2\right]+\left[2\mathbf{N}^2-3\right]\Pi_e^2\omega^2\left[2\omega^2-\Omega_e^2\right]+\\ \left[\mathbf{N}^2-1\right]\omega^2\left[\left(\mathbf{N}^2-2\right)\omega^4-\left(\omega^2-\Omega_e^2\right)^2\right]\end{array}\right)\end{array}\right]}. \quad (14)$$

The derivation of Eq. (14) is summarized in the Appendix. Equation (14) reveals an interesting effect. When the beam propagates perpendicular to the χ-direction ($N_\chi = 0$) Eq. (14) becomes

$$v_{g,\chi} = \frac{c\left(\omega^2 - \Omega_e^2\right)\left(1-\mathbf{N}^2\right)\omega^2\Omega_e^2 B_\chi \mathbf{B}.\mathbf{N}}{\left[\begin{array}{l}\left(1-\mathbf{N}^2\right)\left(\mathbf{B}.\mathbf{N}\right)^2\omega^2\Omega_e^2\left(2\omega^2-\Omega_e^2\right)+ \\ \mathbf{B}^2\left(\begin{array}{l}\Pi_e^4\left[3\omega^2-2\Omega_e^2\right]+\left[2\mathbf{N}^2-3\right]\Pi_e^2\omega^2\left[2\omega^2-\Omega_e^2\right]+ \\ \left[\mathbf{N}^2-1\right]\omega^2\left[\left(\mathbf{N}^2-2\right)\omega^4-\left(\omega^2-\Omega_e^2\right)^2\right]\end{array}\right)\end{array}\right]}, \tag{15}$$

Since the group velocity from Eq. (15) is generally non-zero, this informs us that the beam will "drift" in a direction *perpendicular* to the wave propagation direction. This occurs because of the partial alignment between the wave propagation direction and the local magnetic field i.e. $\mathbf{B}.\mathbf{N} \neq 0$. In tokamaks, the magnetic field has components in all three spatial coordinates (except in some local regions such as the magnetic axis) and so the dot-product $\mathbf{B}.\mathbf{N}$ is usually non-zero. For instance, even when a microwave beam is launched radially ($N_\phi = 0$) it naturally expands. This expansion causes the beam to "see" the poloidal magnetic field component $\mathbf{B}_p$. Hence the beam acquires a group velocity in the toroidal direction without any refractive index gradient in that direction since $\mathbf{B}_p.\mathbf{N}_p$ is non-zero. On the other hand, if the wave propagation direction is perfectly perpendicular to the field, then Eq. (14) becomes

$$v_{g,\chi} = \frac{c\omega^2\left(\omega^2-\Omega_e^2\right)\left(\begin{array}{l}2\left[\Pi_e^2-\omega^2\right]\left[\Pi_e^2+\left(\mathbf{N}^2-1\right)\omega^2\right]+ \\ \left[\Pi_e^2+2\left(\mathbf{N}^2-1\right)\omega^2\right]\Omega_e^2\end{array}\right)}{\Pi_e^2\left(\begin{array}{l}\Pi_e^4\left[3\omega^2-2\Omega_e^2\right]+\left[2\mathbf{N}^2-3\right]\Pi_e^2\omega^2\left[2\omega^2-\Omega_e^2\right]+ \\ \left[\mathbf{N}^2-1\right]\omega^2\left[\left(\mathbf{N}^2-2\right)\omega^4-\left(\omega^2-\Omega_e^2\right)^2\right]\end{array}\right)} N_\chi . \tag{16}$$

As can be seen, when the wave propagates perfectly perpendicular to both the magnetic field and the χ-direction (**B.N** = 0 and N_χ = 0) then the group velocity $v_{g,\chi}$ = 0. We can therefore conclude that the drifts previously discussed are present only when the wave propagates partially parallel to the magnetic field.

These drifts are most pronounced close to the cut-off where the ray refracts and the wave propagation direction partly aligns with the poloidal field. Near the cut-off layer, $N \sim 0$ and the frequency is ω_O, ω_U or ω_L, so the group velocity neatly simplifies to

$$v_{g,\chi,F} \approx c\alpha_F \left(N_\chi + \left(2\varepsilon_F^2 - 1\right)\frac{B_\chi \mathbf{B}.\mathbf{N}}{\mathbf{B}^2} \right), \tag{17}$$

where the subscript F symbolizes O, U or L. We use here a dimensionless scaling term

$$\alpha_F = 1 + \left[\frac{\Pi_e^2 \omega_F \left(\varepsilon_F \omega_F + \Omega_e\right)}{4\Pi_e^4 + 4\Omega_e^3 \varepsilon_F \omega_F + 2\Pi_e^2 \Omega_e \left(2\Omega_e + 5\varepsilon_F \omega_F\right)} - \varepsilon_F \right] \varepsilon_F , \tag{18}$$

with ε_O = 0, ε_U = 1 and ε_L = -1. Since in experimental reflectometry, the wave propagates principally along the R-axis on the plasma mid-plane ($N_\phi << 1$), it is interesting to investigate any resultant toroidal drift. So from Eq. (17) we have

$$v_{g,\phi,F} \approx c\alpha_F \left(2\varepsilon_F^2 - 1\right)\frac{\mathbf{B}_p.\mathbf{N}_p}{\mathbf{B}^2} B_\phi , \tag{19}$$

where the subscript "p" signifies that the vectors are in the poloidal plane (R, Z).

For the ω_O cut-off we obtain

$$v_{g,\phi,O} \approx -c\frac{\mathbf{B}_p.\mathbf{N}_p}{\mathbf{B}^2} B_\phi . \tag{20}$$

If $\mathbf{B}_p$ and $\mathbf{N}_p$ have opposite orientations ($\mathbf{B}_p.\mathbf{N}_p$<0), then the beam will drift toroidally in the co-direction (the direction of $\mathbf{B}_\phi$). On the other hand, if $\mathbf{B}_p$ and $\mathbf{N}_p$ have the same orientation, then the beam will drift in the counter-direction. For ω_U we have

$$v_{g,\phi,U} \approx c\frac{\Pi_e^2\omega_U\left(\omega_U+\Omega_e\right)}{4\Pi_e^4+4\Omega_e^3\omega_U+2\Pi_e^2\Omega_e\left(2\Omega_e+5\omega_U\right)}\frac{\mathbf{B}_p.\mathbf{N}_p}{\mathbf{B}^2}B_\phi . \quad (21)$$

Since the fraction in Eq. (21) is always positive we conclude that if $\mathbf{B}_p$ and $\mathbf{N}_p$ have the same orientation, then the beam will drift in the co-direction. On the other hand, if $\mathbf{B}_p$ and $\mathbf{N}_p$ have opposite orientations, then the beam will drift in the counter-direction. Note that this response is opposite to that observed for ω_O.

For actual reflectometry systems, this drift occurs principally in the toroidal direction. The drift also depends on the orientation of both the toroidal field and the toroidal plasma current. A direct consequence of Eq. (19) is that ω_O and $\omega_{U,L}$ frequency beams will always drift toroidally in opposite directions. Now we complement our description by modeling the beam as a set of multiple rays.

Multiple-ray model

Since it is difficult to picture the resultant beam distortion due to the radial, poloidal and toroidal drifts when simply observing a number of individual ray trajectories, another method to visualize the power flow has been utilized. The *cross-section or returned footprint* of the beam is used to illustrate the distortion as the wave propagates in the plasma. A local Cartesian coordinate system (x, y, z) is employed as shown in Figure 1-a. It is aligned with $\mathbf{B}$ such as $\mathbf{B}$ = (0, 0, B). We use $\mathbf{v}_g = (v_{g,x}, v_{g,y}, v_{g,z})$ and $\mathbf{N} = (N_x, N_y, N_z)$. The group velocity $v_{g,\chi}$ in the χ-direction (χ being now x, y or z) has the following form

$$v_{g,\chi}=\frac{c\omega^2\left(\omega^2-\Omega_e^2\right)\left[\begin{array}{l}2\left(\Pi_e^2-\omega^2\right)\left[\Pi_e^2-\left(1-\mathbf{N}^2\right)\omega^2\right]+\\ \left[\left(1-N_z^2\right)\Pi_e^2-2\left(1-\mathbf{N}^2\right)\omega^2\right]\Omega_e^2+\\ \delta_{\chi z}\left(1-\mathbf{N}^2\right)\Pi_e^2\Omega_e^2\end{array}\right]}{\Pi_e^2\left[\begin{array}{l}\Pi_e^4\left[3\omega^2-2\Omega_e^2\right]+\left[2\mathbf{N}^2-3\right]\Pi_e^2\omega^2\left[2\omega^2-\Omega_e^2\right]+\\ \left[\mathbf{N}^2-1\right]\omega^2\left[\left(\mathbf{N}^2-2-N_z^2\right)\omega^4-\left(1-N_z^2\right)\left(\omega^2-\Omega_e^2\right)^2\right]\end{array}\right]}N_\chi\,. \tag{22}$$

where $\delta_{\chi z}$ is 1 if $\chi = z$ and 0 if $\chi \neq z$. The derivation of Eq. (22) is summarized in the Appendix. If a ray does not propagate in the magnetic field direction ($N_z = 0$) then $v_{g,z} = 0$ and there is no drift in the field direction.

To more clearly illustrate the experimental situation, we focus on a radial beam launch. Since the beam propagates with a shallow range of angles (due to beam divergence) along the *R*-direction, a simple rotation of the coordinate system around the *z*-axis approximately aligns wave propagation to the *x*-coordinate (see Figure 1). To assess distortion of the beam cross-section we then look at the group velocities along the *y*- and *z*-axes and compare beam expansion in the plasma to expansion in vacuum. By looking at the rays traveling at the periphery of the beam we can assess the beam distortion easily. For instance we follow the $1/e^2$-power envelope from the launch. For any beam in vacuum, the phase velocity and the group velocities are collinear and the vacuum expansion of the beam is

$$\frac{v_{g,z}}{v_{g,y}}=\frac{u_z}{u_y} \tag{23}$$

We used the propagation vector direction $\mathbf{u}=(u_x,u_y,u_z)$ defined by

$$\mathbf{u}=\frac{\mathbf{N}}{\sqrt{\mathbf{N}.\mathbf{N}}}\,. \tag{24}$$

The beam cross-section maintains the same symmetrical shape as it expands. In contrast, expansion of the beam in a plasma is determined by taking the ratio of Eq. (22) for both y and z components

$$\frac{v_{g,z}}{v_{g,y}} = \left[1 + \frac{\left(1-\mathbf{N}^2\right)\Pi_e^2\Omega_e^2}{2\left(\Pi_e^2-\omega^2\right)\left[\Pi_e^2-\left(1-\mathbf{N}^2\right)\omega^2\right]+\left[\left(1-N_z^2\right)\Pi_e^2-2\left(1-\mathbf{N}^2\right)\omega^2\right]\Omega_e^2} \right] \frac{u_z}{u_y}. \qquad (25)$$

As expected, for a zero density plasma ($\Pi_e = 0$), Eq. (25) turns into Eq. (23). We now compare the vacuum beam expansion, given by Eq. (23), to the beam expansion in plasma, Eq. (25). If the bracketed term on the RHS of Eq. (25) is larger than 1, the cross-section will elongate in the z-direction (the magnetic field direction). In contrast, if this term is less than 1, the cross-section will expand along the y-axis (perpendicular to the magnetic field).

As discussed previously, the cut-off is the region where the beam experiences the largest distortion and, so, this is where we initially focus attention. First we look at the case where the cutoff frequency is given by $\omega_O = \underline{\Pi}_e$, where $\underline{\Pi}_e$ is the plasma frequency at the cut-off layer. For low-field side launch at a frequency $\omega = \underline{\Pi}_e$, the plasma frequency Π_e varies from 0, at the edge of the plasma, to $\underline{\Pi}_e$, at the cut-off. Close to the cut-off layer, we have $\omega = \underline{\Pi}_e = (1+\varepsilon)\Pi_e$, where ε is an arbitrarily small positive number. We can rewrite Eq. (25) using a Taylor expansion and we get

$$\frac{v_{g,z}}{v_{g,y}} \approx \left[1 - \frac{1}{1+2\varepsilon} \right] \frac{u_z}{u_y}. \qquad (26)$$

Since the bracketed term in Eq. (26) is smaller than 1, beam elongation in the direction perpendicular to the magnetic field is always preferred. Furthermore when rays are extremely close to the cut-off, $v_{g,z}/v_{g,y} \sim 0$, the rays bend only in a direction perpendicular

to the field. The rays cannot propagate and therefore energy cannot flow along the magnetic field at the ω_O cut-off and any trajectory becomes perpendicular to the field at this location[7]. This is clearly illustrated in Figure 3-a. If we approximate the return beam envelope with an ellipse, we see that the major axis of the ellipse is aligned with the perpendicular direction of the total field at the cut-off.

We now look at the ω_U cut-off frequency. As a benign simplification, we assume that the spatial variation of the magnetic field can be neglected compared to the plasma frequency variation near the cut-off region. We use again $\underline{\Pi}_e = (1+\varepsilon)\Pi_e$. Doing so yields

$$\frac{v_{g,z}}{v_{g,y}} \approx \left[1+\frac{1}{1+4\varepsilon\left[1+\sqrt{4\Pi_e^2/\Omega_e^2\left(1+2\varepsilon\right)+1}\right]}\right]\frac{u_z}{u_y}. \qquad (27)$$

Since, in this case, the bracketed term in Eq. (27) is larger than 1, the ω_U cut-off frequency favors elongation in the direction of the magnetic field. When the rays are extremely close to cut-off, $v_{g,z}/v_{g,y} \sim 2u_z/u_y$, and bending occurs in both the z- and y-directions. If we approximate the return beam power envelope with an ellipse we see that the slope of the major axis of the ellipse is approximately twice the pitch angle of the total magnetic field near cut-off.

Away from the cut-off, $\Pi_e << \omega$ for both ω_O and ω_U frequencies and Eq. (25) simplifies to

$$\frac{v_{g,z}}{v_{g,y}} = \left[1-\frac{1}{2}\frac{\Pi_e^2}{\omega^2}\frac{\Omega_e^2}{\Omega_e^2-\omega^2}\right]\frac{u_z}{u_y}. \qquad (28)$$

If we suppose ($\omega - \Omega_e$) finite, then Eq. (28) is equivalent to Eq. (23). The cross-section of the cone of rays remains almost unchanged as the rays propagate in the plasma well away from cutoff.

To summarize this section we conclude that when a circular beam launched into a plasma and reaches a cut-off, the footprint of the returned (i.e. reflected) beam will become elongated. This elongation is primarily dictated by the *field direction at the cut-off*. If we use the ω_O cut-off frequency, the shape will expand perpendicular to the total field direction at the cut-off layer. If we launch an $\omega_{U\text{-}L}$ cut-off frequency, then the axis of the elliptical footprint will tilt in the direction of the magnetic field at the cut-off. In the following section, we provide more detail and numerically confirm these effects.

3D numerical ray tracing calculations in ITER geometry

The preceding sections presented analytical arguments to describe local drift and elongation of a microwave beam near cut-off in a magnetized plasma, where equations can be readily simplified. In this section, we study the interaction between beam and plasma by solving the full ray tracing equations, Eqs. (10) and (11), numerically using the 3D code Genray[8] and ITER[9] geometry and field. It is important to note that our previous conclusions apply to a cold plasma dielectric tensor. Relativistic effects in ITER can be well approximated by correcting the electron mass using[10],

$$m_e \to m_e \sqrt{1 + 5T_e / M_e}\,, \tag{29}$$

where m_e is the electron mass, T_e the electron temperature and M_e = 511 keV is the electron rest mass. This only requires an adjustment of Π_e and Ω_e. This relativistic model does not change the form of the plasma dispersion relation. Furthermore if the

temperature gradient scale length is much larger than the wavelength of the micro-wave beam, Eq. (14) and (22) remain unaltered. While hot plasma dielectric effects are not specifically discussed in this paper, Genray calculations, using the relativistic dielectric tensor, clearly indicate a similar behavior to that described previously.

Our first objective is to compare numerically with the analytical results obtained using Eq. (17). Figure 2 illustrates a radial projection of the beam modeled as a single ray. When the beam is well aligned with the plasma mid-plane, **N**.**B** is null and the numerical results show little drift (see Figure 2 central waveguides). Now if the beam is launched above or below the plasma mid-plane a toroidal drift clearly develops. This drift is non-negligible since it is on the order of the waveguide diameter. A receiver waveguide of equivalent diameter, located above the launch guide, would not intersect the return beam and would fail to capture the return signal. We see the importance in taking account of this toroidal drift when dealing with large tokamaks such as ITER. The drifts presented in Figure 2 correspond to a cutoff location 40 cm from the last closed flux surface (LCFS) which represents only 25 % of the plasma minor radius in ITER. A 15-cm up-down misalignment of the launch relative to the plasma mid-plane has dramatic consequences on the alignment of the return beam. As a result, microwave launch on the plasma mid-plane is preferred in order to maximize the return signal. Many experimental reflectometry setups are designed following this guideline. However setting the launch antenna on the plasma mid-plane does not guarantee maximum signal strength when up-down plasma motion occurs. In ITER vertical plasma displacements of tens of centimeters are anticipated for different operating scenarios and during start-up. It is clear that an antenna array will be required to accommodate such displacements.

To complete our understanding of beam propagation, we consider a multi-ray representation. First we look at the propagation of a beam with circular cross-section launched at the edge of the plasma at a frequency to intersect the ω_O cut-off. Figure 3-a illustrates the orthogonal projection of all the rays onto the (Z, ϕ) plane at the edge of the plasma (i.e. radial view). Figure 3-b presents the same bundle of rays projected on the (R, Z) plane (i.e. toroidal view). The rays propagate 40-cm beyond the LCFS. The colors correspond to the radial position (R) of each ray with red indicating the LCFS and blue the cutoff. The pronounced elongation of the return beam mentioned previously is clearly visible in Figure 3-a. Note that at the cut-off all the rays are oriented perpendicular to the local magnetic field direction. Rays which start at the edge perpendicular to the field direction at the cut-off have a projected trajectory in the (R, ϕ) plane that remains effectively unaltered. In contrast, trajectories of rays launched with projections parallel to the field at the cut-off are significantly modified. As can be seen energy flow parallel to the field direction is not possible at the cut-off. All rays are aligned perpendicular to the field direction at this location, regardless of their initial trajectories. As rays exit the plasma, they form an elliptical footprint on the (Z, ϕ) plane which is offset relative to the center of the launched beam as expected from the toroidal drift previously discussed. However another phenomenon appears. As Figure 4-a shows, the "footprint" of the return beam is tilted due to the "redistribution" of the rays at the cut-off. As the rays are forced to travel perpendicular to the field direction near the cut-off, beam elongation along the field direction becomes impossible. This leads to an elliptical footprint whose major axis is tilted almost exactly perpendicular to the magnetic field direction at cutoff. The receiver antenna design should take account of this effect in order to maximize signal

strength. On the other hand, if this tilt angle could be measured it would be possible to directly determine the magnetic field direction at cut-off. Figure 4-b illustrates the rather accurate correspondence between the actual poloidal field obtained from the MHD equilibrium and from the calculated tilt angle of the beam footprint at the plasma edge. As Eq. (26) shows this tilt is independent of the density profile used (Figure 4-b). When the ω_U cut-off frequency is considered, optimization of the receiving antenna array is more straightforward since the weaker field effects predicted by Eq. (27) do not develop large beam drifts and distortions. Figure 5 shows that, although elongation is observed, the footprint of the return beam is more isotropic and a vertical antenna array would easily accommodate plasma motion and toroidal drifts. As a result we believe X-mode reflectometry to be better suited for core plasma measurements when dealing with large, high-field fusion devices such as ITER.

Conclusion

In this paper, the ray tracing approximation is utilized to model energy flow of microwave radiation in a magnetized tokamak plasma, represented as a cold dielectric medium. Under these conditions, the group velocity of a microwave beam can be computed analytically in both toroidal (Eq. (14)) and Cartesian (Eq. (22)) coordinate systems for a tokamak plasma. Focusing on reflectometry techniques, the existence of an inevitable drift of the beam (energy flow) in a direction perpendicular to the direction of wave propagation was identified. This behavior occurs when the propagation vector **k** (or **N**) partially aligns with the magnetic field. This always occurs during reflectometry measurements on a tokamak plasma due to inherent beam divergence and the magnetic field helicity. In the case of an experimental set-up where the beam initially propagates

primarily in the poloidal plane, it was demonstrated that the presence of the poloidal magnetic field $\mathbf{B_p}$ is sufficient to explain the drift of the beam in the toroidal direction. This drift occurs independent of any refractive index gradient in the toroidal direction and is most pronounced near the cut-off, where reflection forces alignment between $\mathbf{N}$ and $\mathbf{B_p}$. Since N is negligible near the cut-off, Eq. (14) simplifies into Eq. (20) for an O-mode cut-off and Eq. (21) for an X-mode cut-off. These equations clearly illustrate a different response for the two polarizations. In general, O-mode and X-mode beams drift toroidally in opposite directions. The O-mode drift is the most pronounced.

When beam divergence is taken into account in the model, distortion of the beam cross section also appears. To understand the physical reasons for this phenomenon, Eq. (22) was transformed into Eq. (25). This equation gives the distortion of the beam cross-section as it progresses radially in the plasma. Once again analysis of O-mode and X-mode polarization indicate a quite different response. The beam distortion for an O-mode cut-off is elongated in the direction perpendicular to the magnetic field while the distortion for an X-mode cut-off is more pronounced along the field direction. In general the "footprint" of the return beam can be well approximated by an ellipse which tends to align parallel (X-mode) or perpendicular (O-mode) to the magnetic field direction. Near the cut-off, the simplified Eq. (26) and (27) can be used. A remarkable trait of Eq. (26) is that O-mode polarization cannot have any group velocity along the direction of the total magnetic field at the cut-off. This effect is illustrated clearly in Figure 3-a. The reader should note that absence of a group velocity in the total field direction is not incompatible with the presence of a toroidal group velocity since the total magnetic field is not in the toroidal direction (except at the magnetic axis). A direct consequence of this result is that

the major axis of the elliptical beam cross-section is aligned exactly perpendicular to the field direction at the cut-off. A similar effect also exists for X-mode, where the major axis of the ellipse tilts towards the magnetic field direction although never aligns perfectly with it. The use of the ray tracing code Genray confirmed the analytical predictions of beam "stirring" and distortion due to the wave propagation misalignment with the internal magnetic field. These effects are magnified in large, high-field machines and should not be ignored when designing any microwave system. Finally, the numerical calculations indicate that the direction of the field at cutoff is directly linked to the elliptical footprint of the reflected microwave beam, suggesting that reflectometry might be able to determine the radial profile of magnetic field pitch angle. It is important to note that ray-tracing approximation ignores wave front modulation caused by plasma micro-turbulence[11,12]. This effect could have a significant impact on the "footprint" shape and orientation. This will be the topic of future full-wave code analysis. However ITER will run in the high confinement mode (H-mode) regime and density fluctuation levels will be drastically reduced compared to the low confinement (L-mode) regime. As a consequence, the overall effect on the footprint may be negligible. If successful, information gained from such an approach would complement other magnetic field pitch angle measurement techniques such as motional Stark effect which are extremely challenging in ITER.

Acknowledgements

One of the authors (P.-A.G.) would like to thank A. Smirnov and R. Harvey for the useful discussions regarding toroidal beam drifts and their help in running GENRAY. This research was supported by **PPPL Subcontract #S006786-F.**

Appendix

Computation of the group velocity in cylindrical coordinates

Starting from

$$\mathbf{v}_g = -\frac{\partial D/\partial \mathbf{k}}{\partial D/\partial \omega} = -\frac{\partial \omega}{\partial \mathbf{k}}, \tag{A1}$$

where the group velocity is defined by

$$\mathbf{v}_g = \left(\frac{dR}{dt}, \frac{dZ}{dt}, R\frac{d\phi}{dt} \right). \tag{A2}$$

We can rewrite Eq. (A1) into

$$\mathbf{v}_g = -\frac{c}{\omega}\frac{\partial D/\partial \mathbf{N}}{\partial D/\partial \omega}, \tag{A3}$$

Since we use a cylindrical coordinate system we use

$$\frac{\partial D}{\partial \mathbf{N}} = \left(\frac{\partial D}{\partial M_R}, \frac{\partial D}{\partial M_Z}, R\frac{\partial D}{\partial M_\phi} \right), \tag{A4}$$

We write symbolically $M_R = N_\mathrm{R}$, $M_Z = N_Z$ and $M_\phi = RN_\phi$. First we focus on the numerator of Eq. (A3) for any coordinate χ,

$$\frac{\partial D}{\partial M_\chi} = \frac{\partial A}{\partial M_\chi} N^4 + 2AN^2 \frac{\partial N^2}{\partial M_\chi} - \frac{\partial B}{\partial M_\chi} N^2 - B\frac{\partial N^2}{\partial M_\chi} + \frac{\partial C}{\partial M_\chi}. \tag{A5}$$

We can readily compute

$$\frac{\partial N^2}{\partial M_\chi} = 2\frac{M_\chi}{R_\chi}. \tag{A6}$$

To get homogeneous formulas we used the symbol R_χ which is 1 when $\chi = R$ or Z and is equal to R when $\chi = \phi$. We now look at the A, B and C terms.

$$\begin{cases} \dfrac{\partial A}{\partial M_\chi} = \left[K_\perp \dfrac{\partial \sin^2\theta}{\partial M_\chi} + K_\parallel \dfrac{\partial \cos^2\theta}{\partial M_\chi} \right] \\ \dfrac{\partial B}{\partial M_\chi} = \left[\left(K_\perp^2 - K_\times^2 \right) \dfrac{\partial \sin^2\theta}{\partial M_\chi} + K_\parallel K_\perp \dfrac{\partial \cos^2\theta}{\partial M_\chi} \right] \\ \dfrac{\partial C}{\partial M_\chi} = 0 \end{cases} . \tag{A7}$$

Using the properties of the cosine function we can rewrite Eq. (A7)

$$\begin{cases} \dfrac{\partial A}{\partial M_\chi} = \left[K_\parallel - K_\perp \right] \dfrac{\partial \cos^2\theta}{\partial M_\chi} \\ \dfrac{\partial B}{\partial M_\chi} = \left[K_\parallel K_\perp - K_\perp^2 + K_\times^2 \right] \dfrac{\partial \cos^2\theta}{\partial M_\chi} \end{cases} , \tag{A8}$$

where

$$\frac{\partial \cos^2\theta}{\partial M_\chi} = \frac{2\mathbf{B}.\mathbf{N}\left(R_\chi B_\chi \mathbf{N}^2 - \mathbf{B}.\mathbf{N} M_\chi \right)}{R_\chi^2 \mathbf{B}^2 \mathbf{N}^4} , \tag{A9}$$

Using Eq. (A8) and (A9) in Eq. (A5) and some algebra we get

$$\frac{\partial D}{\partial M_\chi} = \frac{-2}{R_\chi \mathbf{B}^2 \omega^2 \left(\omega^2 - \Omega_e^2 \right)} \begin{bmatrix} \mathbf{B}.\mathbf{N}\left(B_\chi \left[1 - \mathbf{N}^2 \right] - N_\chi \mathbf{B}.\mathbf{N} \right) \Omega_e^2 \Pi_e^2 + \\ \mathbf{B}^2 N_\chi \left(\begin{matrix} 2\left[\Pi_e^2 - \omega^2 \right] \left[\Pi_e^2 + \left(\mathbf{N}^2 - 1 \right) \omega^2 \right] + \\ \left[\Pi_e^2 + 2\left(\mathbf{N}^2 - 1 \right) \omega^2 \right] \Omega_e^2 \end{matrix} \right) \end{bmatrix} . \tag{A10}$$

We now look at

$$\frac{\partial D}{\partial \omega} = \frac{\partial A}{\partial \omega} N^4 - \frac{\partial B}{\partial \omega} N^2 + \frac{\partial C}{\partial \omega} , \tag{A11}$$

where

$$\left|\begin{array}{l}\dfrac{\partial A}{\partial \omega}=\left[\dfrac{2\Pi_e^2\omega}{(\omega^2-\Omega_e^2)^2}\left[1-\dfrac{(\mathbf{N}.\mathbf{B})^2}{\mathbf{N}^2\mathbf{B}^2}\right]+\dfrac{2\Pi_e^2}{\omega^3}\dfrac{(\mathbf{N}.\mathbf{B})^2}{\mathbf{N}^2\mathbf{B}^2}\right] \\ \dfrac{\partial B}{\partial \omega}=\left[\begin{array}{l}\dfrac{4\Pi_e^2\omega^4+\Pi_e^4(2\Omega_e^2-4\omega^2)}{\omega^3(\omega^2-\Omega_e^2)^2}\left[1-\dfrac{(\mathbf{N}.\mathbf{B})^2}{\mathbf{N}^2\mathbf{B}^2}\right]+ \\ \dfrac{2\Pi_e^2\left[\omega^4+(\Omega_e^2-\omega^2)^2+\Pi_e^2(\Omega_e^2-4\omega^2)\right]}{\omega^3(\omega^2-\Omega_e^2)^2}\left(1+\dfrac{(\mathbf{N}.\mathbf{B})^2}{\mathbf{N}^2\mathbf{B}^2}\right)\end{array}\right] \\ \dfrac{\partial C}{\partial \omega}=\dfrac{2\Pi_e^2\left[\Pi_e^4+(3\omega^2-2\Omega_e^2)+\omega^2\Pi_e^2(3\Omega_e^2-6\omega^2)+\omega^2\left(2\omega^2+\left[\omega^2-\Omega_e^2\right]^2\right)\right]}{\omega^5(\omega^2-\Omega_e^2)^2}\end{array}\right. . \qquad \text{(A12)}$$

After some algebra we finally find

$$\frac{\partial D}{\partial \omega}=\frac{2\Pi_e^2}{\mathbf{B}^2\omega^5\left(\omega^2-\Omega_e^2\right)^2}\left[\begin{array}{l}\left(1-\mathbf{N}^2\right)\left(\mathbf{B}.\mathbf{N}\right)^2\omega^2\Omega_e^2\left(2\omega^2-\Omega_e^2\right)+ \\ \mathbf{B}^2\left(\begin{array}{l}\Pi_e^4\left[3\omega^2-2\Omega_e^2\right]+\left[2\mathbf{N}^2-3\right]\Pi_e^2\omega^2\left[2\omega^2-\Omega_e^2\right]+ \\ \left[\mathbf{N}^2-1\right]\omega^2\left[\left(\mathbf{N}^2-2\right)\omega^4-\left(\omega^2-\Omega_e^2\right)^2\right]\end{array}\right)\end{array}\right]. \qquad \text{(A13)}$$

When we put Eq. (A10) and (A13) into Eq. (A3) we obtain

$$v_{g,\chi}=\frac{c\omega^2\left(\omega^2-\Omega_e^2\right)\left[\begin{array}{l}\mathbf{B}.\mathbf{N}\left(B_\chi\left[1-\mathbf{N}^2\right]-N_\chi\mathbf{B}.\mathbf{N}\right)\Omega_e^2\Pi_e^2+ \\ \mathbf{B}^2N_\chi\left(\begin{array}{l}2\left[\Pi_e^2-\omega^2\right]\left[\Pi_e^2+\left(\mathbf{N}^2-1\right)\omega^2\right]+ \\ \left[\Pi_e^2+2\left(\mathbf{N}^2-1\right)\omega^2\right]\Omega_e^2\end{array}\right)\end{array}\right]}{\Pi_e^2\left[\begin{array}{l}\left(1-\mathbf{N}^2\right)\left(\mathbf{B}.\mathbf{N}\right)^2\omega^2\Omega_e^2\left(2\omega^2-\Omega_e^2\right)+ \\ \mathbf{B}^2\left(\begin{array}{l}\Pi_e^4\left[3\omega^2-2\Omega_e^2\right]+\left[2\mathbf{N}^2-3\right]\Pi_e^2\omega^2\left[2\omega^2-\Omega_e^2\right]+ \\ \left[\mathbf{N}^2-1\right]\omega^2\left[\left(\mathbf{N}^2-2\right)\omega^4-\left(\omega^2-\Omega_e^2\right)^2\right]\end{array}\right)\end{array}\right]}. \qquad \text{(A14)}$$

Computation of the group velocity in Cartesian coordinates

We use the local Cartesian coordinate system (x, y, z) given in Figure 1-a and aligned with **B** such as **B** = (0, 0, B). We will stay general by using $\mathbf{v}_g = (v_{g,x}, v_{g,y}, v_{g,z})$ and $\mathbf{N} = (N_x, N_y, N_z)$. Starting once again from Eq. (A1) where the group velocity is now

$$\mathbf{v}_g = \left(\frac{dx}{dt}, \frac{dy}{dt}, \frac{dz}{dt} \right), \tag{A15}$$

we compute

$$\frac{\partial D}{\partial \mathbf{N}} = \left(\frac{\partial D}{\partial N_x}, \frac{\partial D}{\partial N_y}, \frac{\partial D}{\partial N_z} \right). \tag{A16}$$

Again we have,

$$\frac{\partial D}{\partial N_\chi} = \frac{\partial A}{\partial N_\chi} N^4 + 2AN^2 \frac{\partial N^2}{\partial N_\chi} - \frac{\partial B}{\partial N_\chi} N^2 - B \frac{\partial N^2}{\partial N_\chi}. \tag{A17}$$

with χ being now x, y or z and

$$\begin{vmatrix} \frac{\partial A}{\partial N_\chi} = \left[K_\parallel - K_\perp \right] \frac{\partial \cos^2 \theta}{\partial N_\chi} \\ \frac{\partial B}{\partial N_\chi} = \left[K_\parallel K_\perp - K_\perp^2 + K_\times^2 \right] \frac{\partial \cos^2 \theta}{\partial N_\chi} \end{vmatrix}. \tag{A18}$$

Since **B** is along the z-direction only we find

$$\frac{\partial \cos^2 \theta}{\partial N_\chi} = -\frac{2N_\chi N_z^2}{\mathbf{N}^4} + \delta_{\chi z} \frac{2N_z}{\mathbf{N}^2}, \tag{A19}$$

where $\delta_{\chi z}$ is 1 if $\chi = z$ and 0 if $\chi \neq z$. So we have

$$\frac{\partial D}{\partial N_\chi} = \frac{-2N_\chi}{\omega^2\left(\omega^2-\Omega_e^2\right)}\begin{bmatrix} 2\left(\Pi_e^2-\omega^2\right)\left[\Pi_e^2-\left(1-\mathbf{N}^2\right)\omega^2\right]+ \\ \left[\left(1-N_z^2\right)\Pi_e^2-2\left(1-\mathbf{N}^2\right)\omega^2\right]\Omega_e^2+ \\ \delta_{\chi z}\left(1-\mathbf{N}^2\right)\Pi_e^2\Omega_e^2 \end{bmatrix}. \tag{A20}$$

Using Eq. (A13) and after some algebra we obtain

$$v_{g,\chi} = \frac{c\omega^2\left(\omega^2-\Omega_e^2\right)\begin{bmatrix} 2\left(\Pi_e^2-\omega^2\right)\left[\Pi_e^2-\left(1-\mathbf{N}^2\right)\omega^2\right]+ \\ \left[\left(1-N_z^2\right)\Pi_e^2-2\left(1-\mathbf{N}^2\right)\omega^2\right]\Omega_e^2+ \\ \delta_{\chi z}\left(1-\mathbf{N}^2\right)\Pi_e^2\Omega_e^2 \end{bmatrix}}{\Pi_e^2\begin{bmatrix} \Pi_e^4\left[3\omega^2-2\Omega_e^2\right]+\left[2\mathbf{N}^2-3\right]\Pi_e^2\omega^2\left[2\omega^2-\Omega_e^2\right]+ \\ \left[\mathbf{N}^2-1\right]\omega^2\left[\left(\mathbf{N}^2-2-N_z^2\right)\omega^4-\left(1-N_z^2\right)\left(\omega^2-\Omega_e^2\right)^2\right] \end{bmatrix}} N_\chi . \tag{A21}$$

[1] C. Laviron, A. J. H. Donne, M. E. Manso, *et al*., Plasma Phys. Cont. Fusion **38**, 905 (1996)
[2] M. Gilmore, W. A. Peebles, X. V. Nguyen, Rev. Scientific Inst. **70**, 1085 (1999)
[3] E. J. Doyle, R. J. Groebner, K. H. Burrell, *et al*., Phys. Fluids **B 3**, 2300 (1991)
[4] M. Hirsch, E. Holzhauer, J. Baldzuhn, *et al*., Plasma Phys. Cont. Fusion **43**, 1641 (2001)
[5] T. H. Stix, Waves in Plasmas, Springer-Verlag, New York (1992)
[6] L. D. Landau, E. M. Lifshitz, The Classical Theory of Fields, Addison-Wesley, Reading, Massachusetts, 1951
[7] V. L. Ginzburg, Propagation of electromagnetic waves in plasma, p. 582, Gordon and Breach, New York (1961)
[8] A.P. Smirnov, R.W. Harvey, K. Kupfer, Bull Amer. Phys. Soc. **39**, 1626 (1994)
[9] ITER Technical Basis 2002 ITER EDA Documentation Series (Vienna: IAEA)
[10] H. Bindslev, Plasma Phys. Cont. Fusion **35**, 1093 (1993).
[11] E. Z. Gusakov, A. Y. Popov, Plasma Phys. Control. Fusion **44**, 2327 (2002)
[12] E. Z. Gusakov, A. V. Surkov, A. Y. Popov, Plasma Phys. Control. Fusion **47**, 959 (2005)

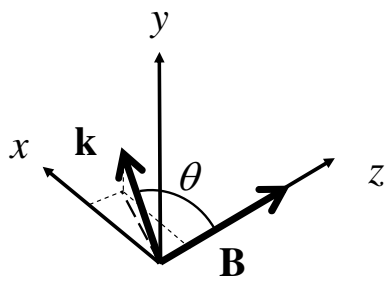

Figure 1. Magnetic field B, propagation vector k in the local orthogonal coordinate system (*x*, *y*, *z*). The k vector points mainly in the *x*-direction.

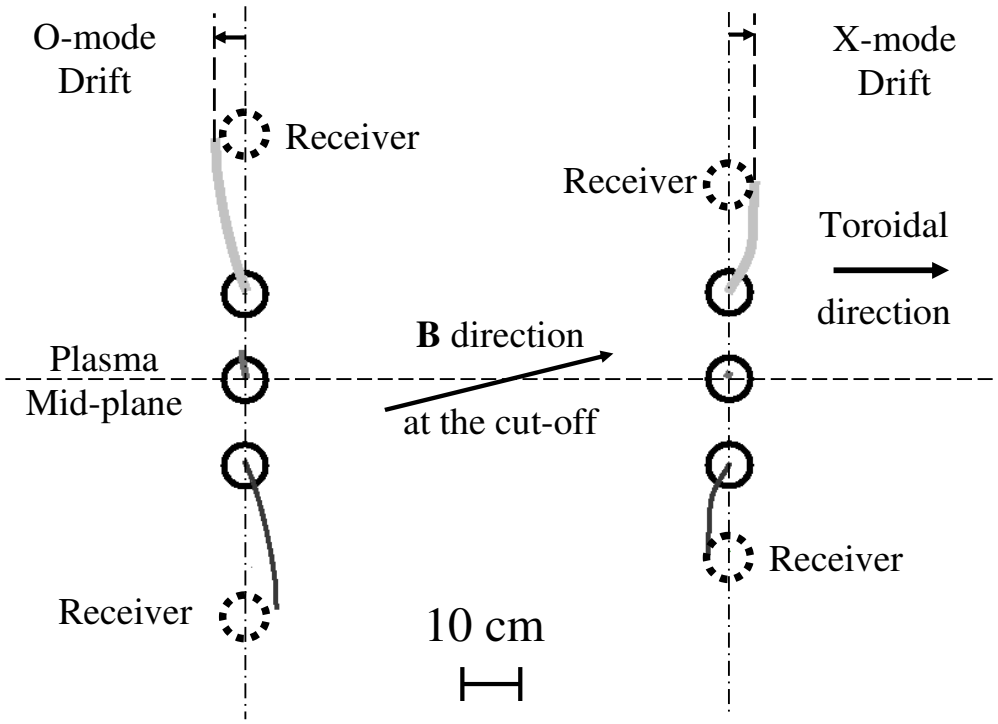

Figure 2. Radial projection (looking at the plasma edge from the magnetic axis) of incident and reflected microwave rays for O-mode and X-mode reflectometry with a cut-off layer 40 cm past the last closed flux surface. The density profile used corresponds to Profile 2, given in Figure 4-b. The continuous lines represent the rays launched from different waveguide antenna (circles) at three different heights. The middle waveguides are on the plasma mid-plane (represented by the horizontal dashed line) where the rays are almost perpendicular to the magnetic field. This corresponds to an ideal experimental launch since toroidal drifts are minimal. As we move above or below the mid plane, toroidal drifts occur due to the loss of orthogonality between wave propagation and magnetic field.

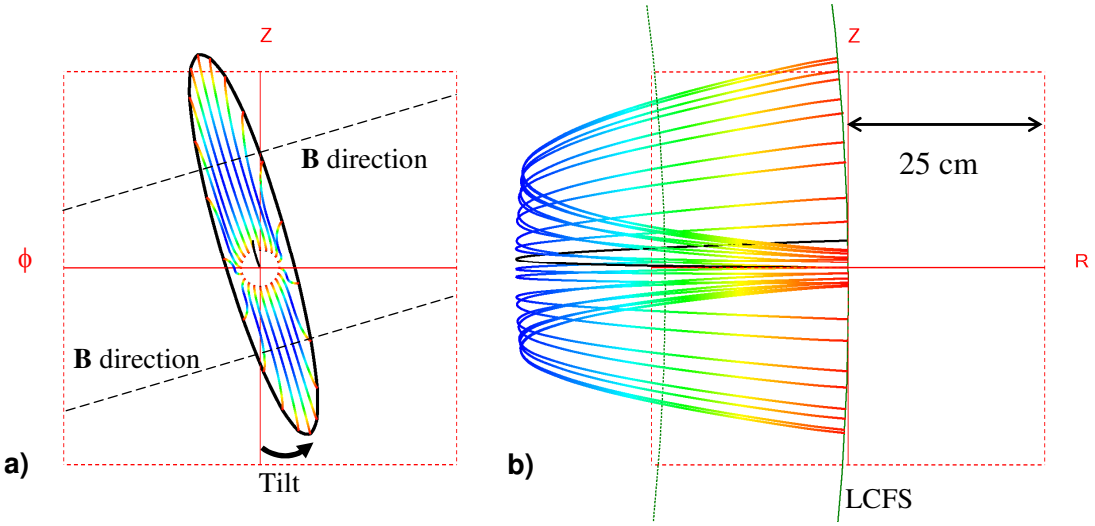

Figure 3. (color online) a) Radial and b) poloidal projections for O-mode propagation (90 GHz) 40 cm deep in the plasma. The central ray is in black. The return footprint on the (Z, ϕ) plane resulting from the $1/e^2$ launch envelope is shown in Figure 3-a. The direction of the total magnetic field at the cut-off is shown in Figure 3-a.

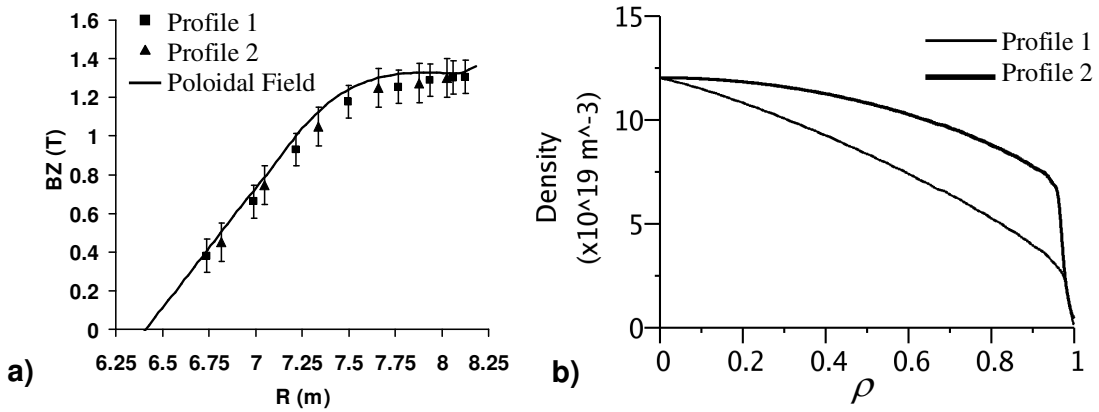

Figure 4. a) Poloidal field and corresponding b) density profiles. The poloidal field found from the equilibrium file (solid line) and the poloidal field computed from the tilt of the return beam footprint (triangles, squares) match very well,and are independent of the shape of the density profile. To obtain the poloidal field from the tilt, the slope of the major axis of the footprint is measured. This slope gives directly the ratio between the poloidal and toroidal fields at the cut-off. Since the toroidal field is well known across the whole profile, a rather accurate value of the poloidal field can be inferred. ρ is the normalized poloidal flux coordinate (0 on the axis and 1 at the edge).

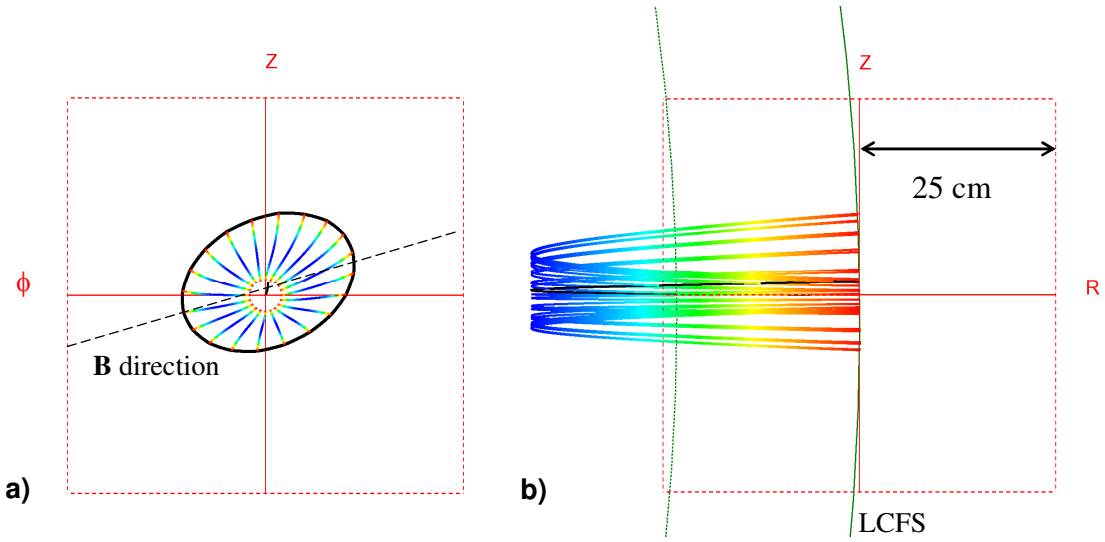

Figure 5. (color online) a) Radial and b) poloidal projections for X-mode propagation (171 GHz) 40 cm deep in the plasma using the conventions listed in Figure 3.